energies

MDPI

Article

Multi-Parameter Optimization Analysis of Hydrodynamic Performance for Rim-Driven Thruster

Yuanzhe Nie [1], Wu Ouyang [2,3,4,*], Zhuo Zhang [2], Gaoqiang Li [1] and Ruicong Zheng [2,5]

[1] School of Naval Architecture, Ocean and Energy Power Engineering, Wuhan University of Technology, Wuhan 430063, China
[2] School of Transportation and Logistics Engineering, Wuhan University of Technology, Wuhan 430063, China
[3] Reliability Engineering Institute, National Engineering Research Center for Water Transport Safety, Wuhan 430063, China
[4] East Lake Laboratory, Wuhan 420202, China
[5] Guangzhou Haigong Marine Equipment Co., LTD., Guangzhou 510000, China
* Correspondence: ouyangw@whut.edu.cn

Abstract: The efficiency of rim-driven thrusters (RDT) has always been the focus of attention in the context of energy conservation and environmental protection. A multi-parameter collaborative optimization framework is proposed to improve the efficiency of RDT based on the response surface method (RSM). The common structural parameters of RDT, including pitch ratio, disk ratio and rake angle, are selected as design variables to carry out the Box–Behnken experimental design combined with the simulation data obtained through CFD calculations. The response surface second-order model is employed to evaluate the extent to which different parameters can affect the target variable and obtain the optimal hydraulic efficiency. The results show that the established model has high precision, good reproducibility and strong anti-interference ability. The influence of the pitch ratio, rake angle and disk ratio on open water efficiency decreases in sequence. Compared with the prototype RDT, the maximum efficiency of the optimized RDT is increased by 13.8%, and the surface pressure distribution and flow field characteristics are also significantly modified.

Keywords: rim-driven thrusters (RDT); response surface method (RSM); hydrodynamic performance; computational fluid dynamics (CFD); multi-parameter optimization

Citation: Nie, Y.; Ouyang, W.; Zhang, Z.; Li, G.; Zheng, R. Multi-Parameter Optimization Analysis of Hydrodynamic Performance for Rim-Driven Thruster. *Energies* **2023**, *16*, 891. https://doi.org/10.3390/en16020891

Academic Editor: Biswajit Basu

Received: 2 December 2022
Revised: 9 January 2023
Accepted: 10 January 2023
Published: 12 January 2023

1. Introduction

With the development of intelligent and green ships, the problems of traditional mechanical propulsion systems are becoming increasingly prominent, which cannot meet the increasingly strict emission regulations proposed by the International Maritime Organization (IMO) for ship propulsion systems [1]. As an alternative propulsion scenario of the mechanical propulsion system, the electric propulsion system has shown great potential in energy conservation and environmental protection [2]. Furthermore, the breakthrough of power electronics and motor control technology and the application of new semiconductor materials have prompted the electric propulsion device to derive a variety of forms to cope with the requirements of different ship types in recent years. In this context, rim-driven thrusters (RDT) designed according to the concept of modularization have become the focus of people's attention with their innovative structure and are expected to be widely used in the future [3].

The integrated electric propulsion device embeds the blade tip and the rotor together to facilitate a motor to drive the blades directly, which can minimize the loss of energy transmission. Simultaneously, both sides of the rim are fixed and supported by water-lubricated bearings to omit the cooling and lubrication system [4]. All components are installed in the duct to form a compact integrated unit, effectively reducing the space

occupancy and allowing flexible installation and arrangement. The structure of RDT is shown in Figure 1.

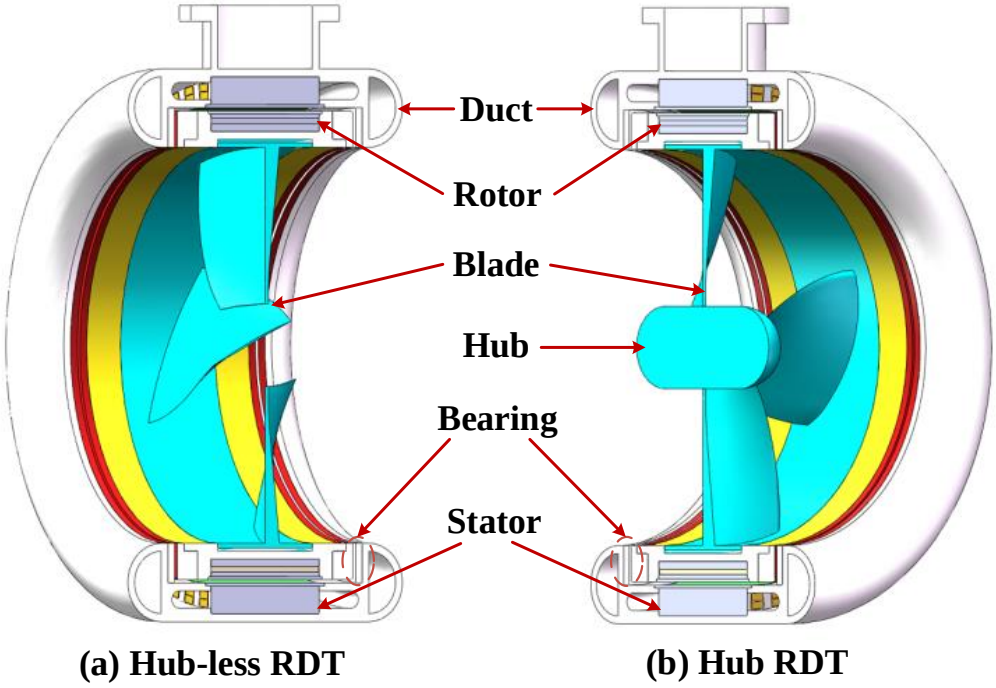

Figure 1. RDT structures.

Due to the special structure and many advantages of RDT, there has been much research on its hydrodynamic performance, involving flow field characteristics, vibration and noise, scale effect and cavitation performance. Zhu et al. [5] explored the internal flow characteristics of RDT and revealed its flow loss mechanism. Freeman et al. [6] analyzed the pressure distribution, incoming flow and vibration frequency of RDT blades based on the fine element analysis (FEA). Chen et al. [7] compared the longitudinal vibration and unsteady thrust transmission characteristics of shaftless rim-driven thrusters and traditional shaft-driven propellers. Jiang et al. [8] discussed the flow distribution characteristics of gap fluid in counter-rotating shaftless RDT (CRP-RDT) and the influence of a gap on its hydrodynamic performance. Yang et al. [9] investigated the scale effect of RDT components in consideration of the interaction between the duct and the rim.

As mentioned above, the performance research of RDT is almost accomplished through numerical calculations. Accordingly, some innovative calculation methods have been adopted to deal with the contradictions between efficiency and accuracy. Kinnas et al. [10] employed a novel method to predict the effective wake and cavitation degree of RDT, which combines a vortex lattice method (MPUF-3A) with a RANS Solver (FLUENT) for an unsteady flow analysis. Cai et al. [11] proposed a modified body force method to calculate the self-propulsion performance of matching RDT ships. Compared with the discrete propeller method, this method can save a lot of computing resources on the premise of ensuring accuracy. Hieke et al. [12] provided a hybrid procedure for the hydroacoustic calculations and analysis of RDT, in which the transient pressure and velocity obtained by the stress-blended eddy simulation (SBES) are used as the initial conditions to calculate the underwater acoustic field based on the expansion about the incompressible flow (EIF) approach and coherent flow structures were filtered through the proper orthogonal decomposition (POD) method.

However, it is difficult to satisfy the requirements of green intelligent ships for propulsion devices only through performance research. At present, some problems confronted with the development of RDT, such as low hydraulic efficiency, underwater noise and ship–propeller matching, need to be overcome through structural optimization design. As far as

RDT hydraulic components are concerned, quite some studies have analyzed the single parameter effects of blades, ducts and rims. Zhang et al. [13] and Xiangcheng et al. [14] investigated some of the primary factors affecting the hydrodynamic performance of RDT through simulation, including the number of blades, the length–diameter ratio of the duct, the diffusion ratio, the contract ratio of the duct and the tip diameter ratio of the blade. Cao et al. [15] analyzed the wake field, blade load distribution and hydrodynamics of four RDTs with different pitch ratios. Liu et al. [16] compared the hydrodynamic performance and flow field structures of RDT with three different duct designs using the two-equation SST *k*-ω model and the four-equation $\gamma-\mathrm{Re}_\theta$ transition model, respectively. Cai et al. [17] analyzed the influence of the rim length on the wake flow field and friction loss and the influence of the blade thickness on the RDT efficiency. Gaggero [18] proposed an RDT design optimization (SBDO) method based on CFD to explore the impact of the number of blades on the RDT performance through the parametric description of the RDT blades and the use of multi-objective optimization algorithms to maximize blade efficiency and minimize the cavitation. For the influence of the hub, Song et al. [19] designed four pairs of hub types and hub rim-driven thrusters with different hub radii and mainly discussed their open water performance.

To sum up, the existing works focused on the performance and single-parameter optimization designs and lacked research on multi-parameter collaborative optimization for the hydrodynamic performance of RDT. However, due to the integrity of the RDT structure, its hydrodynamic performance is characterized by the interaction of many parameters. Additionally, there is a mutual constraint mechanism between these structural parameters. In most cases, the optimization of a single structural parameter cannot effectively improve the performance of the thruster.

In this study, a multi-parameter collaborative optimization framework for RDT is proposed based on the response surface method. The common structural parameters of the blade, including disk ratio, pitch ratio and rake angle, are selected as design variables to carry out the Box–Behnken experimental design combined with the simulation data obtained through the CFD method. The response surface second-order model is employed to evaluate the extent to which different parameters can affect the target variable and obtain the optimal hydraulic efficiency. Subsequently, the surface pressure distribution and flow field characteristics are also compared between the prototype RDT and the optimized RDT.

2. Methodology

2.1. Design of the RDT

The specific object selected is a 20 kW RDT, and some of its main parameters are shown in Table 1. The modified Ka4-70 blade is used for the propulsion device, in which the profile is an airfoil type from 0.2 R to 0.5 R, and the profile is a bow type from 0.6 R to 1.0 R. Considering the strength requirements of the blade root, the hub is used for supporting and fixing to avert the deformation of the blade root that has a greater impact on the hydraulic efficiency. The designed RDT are shown in Figure 2.

Table 1. Main parameters of the RDT.

Parameter	Representation	Value
Diameter of blade tip circle	D/mm	260
Hub diameter ratio	XH	0.1
Number of blades	N	4
Disc ratio	ARE	0.75
side bevel	$\theta/(^\circ)$	40
Pitch ratio at 0.7 R	P/D	1.2
Rotation speed	n/rpm	880

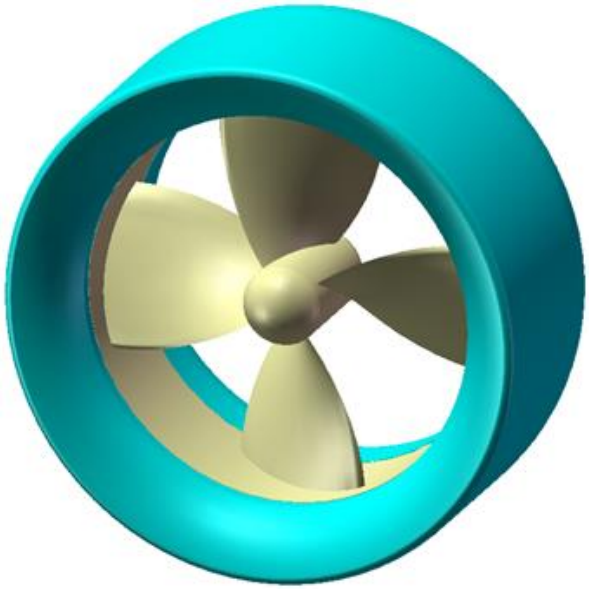

Figure 2. RDT model.

2.2. Numerical Method

2.2.1. Numerical Model

The Reynolds-Averaged Navier–Stokes (RANS) equations are used to solve the flow field based on the assumption of an incompressible and steady flow. The continuity and momentum equations in star ccm+ can be expressed as [20]:

$$\begin{cases} \nabla \cdot \overline{v} = 0 \\ \nabla \cdot (\rho \overline{v} \otimes \overline{v}) = -\nabla \cdot \overline{p} \boldsymbol{I} + \nabla \cdot \left(\overline{\boldsymbol{T}} + \overline{\boldsymbol{T}}_{RANS} \right) + \boldsymbol{f}_b \end{cases} \tag{1}$$

where ρ is the density, $\overline{v}$ is the average velocity, $\overline{p}$ is the average pressure, $\boldsymbol{I}$ is the unit tensor, $\overline{\boldsymbol{T}}$ is the average viscous stress tensor, and $\boldsymbol{f}_{\mathrm{b}}$ is the resultant force of volume force (such as gravity and centrifugal force).

Equation (1) is solved by using the finite volume method, where the SIMPLE algorithm deals with the coupling of pressure and velocity. To ensure the computation speed and convergence, the underrelaxation factors of velocity and pressure are set to 0.7 and 0.3, respectively. The first-order upwind scheme is selected to discretize the partial differential equations. Moreover, the SST k-ω turbulence model developed by Menter is adopted to solve the stress term in the RANS equations, as it improves the boundary layer performance of the k-ε model under strong an adverse pressure gradient and the sensitivity of the k-ω model to the change of the turbulent kinetic energy in the free stream [21]. In the model, the turbulent kinetic energy k and the specific dissipation rate ω solved by the transport equations are introduced to determine the eddy viscosity coefficient μ_t. The SST k-ω turbulence model can be listed as follows [21]:

$$\begin{cases} \frac{\partial}{\partial x_i}(\rho k u_i) = \frac{\partial}{\partial x_j}\left(\Gamma_k \frac{\partial k}{\partial x_j} \right) + G_k - Y_k + S_k \\ \frac{\partial}{\partial x_i}(\rho \omega u_i) = \frac{\partial}{\partial x_j}\left(\Gamma_\omega \frac{\partial \omega}{\partial x_j} \right) + G_\omega - Y_\omega + D_\omega + S_\omega \end{cases} \tag{2}$$

where G_ω is the turbulence influence term, G_k is the turbulent kinetic energy, Y_k and Y_ω are the divergent terms of k and ω, respectively, Γ_k and Γ_ω are the effective diffusion terms of k and ω, respectively, S_k and S_ω are the user-defined functions, and D_ω is the orthogonal divergence term.

2.2.2. Boundary Setup and Grid Generation

A cylindrical computational domain shown in Figure 3 is used to describe the flow field where the RDT is located. The whole flow field is divided into a rotating domain, including hub, blades, rim and inner surface of the duct and a static domain composed of other parts. A Cartesian coordinate system is defined to determine the sizes and positions of different computational domains, which take the blade center as the origin O and the negative direction of the z-axis as the free flow direction. The inlet of the static domain with a radius of $5D$ is located at $6D$ upstream of RDT, and the outlet is located at $8D$ downstream of RDT, where D is the diameter of the blade. The interface between the rotation domain and the static domain is located in the middle of the duct to exchange information between different domains. Table 2 summarizes the boundary conditions of the computational domains.

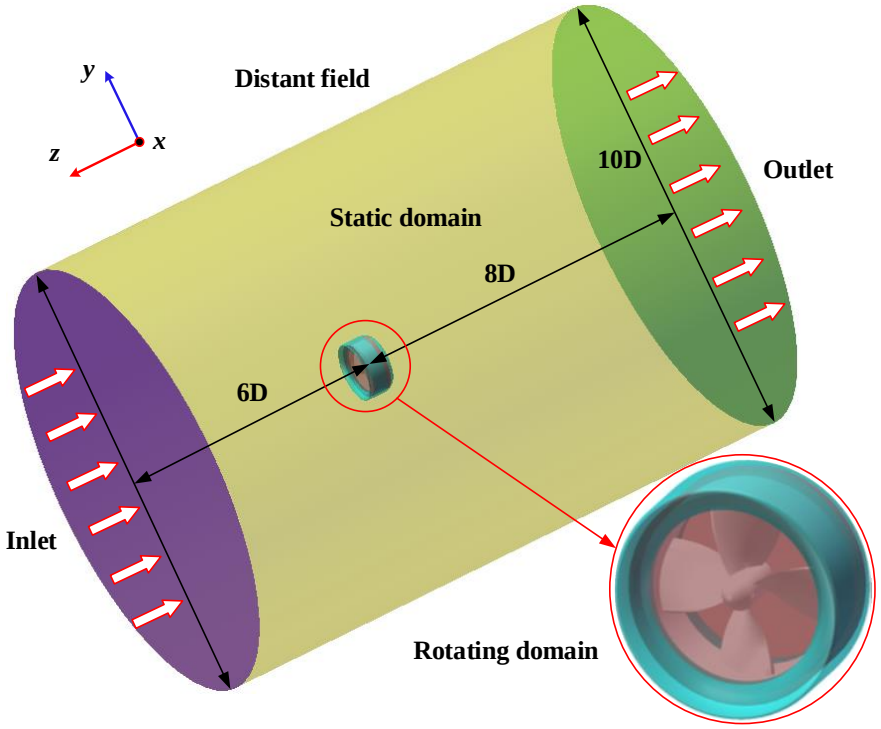

Figure 3. Computational domain for the RDT simulation.

Table 2. Boundary conditions of the computational domains.

	Velocity (m/s)	**Pressure (Pa)**	k **(m^2/s^2)**	ω **(1/s^2)**	μ_t **(Pa·s)**
Inlet	Depends on advance coefficient J	$\frac{\partial p}{\partial n} = 0$	Depends on turbulence intensity (0.01)	Depends on turbulence intensity (0.01) and turbulence viscosity ratio	Calculated
Outlet	$\frac{\partial v}{\partial n} = 0$	Reference pressure	$\frac{\partial k}{\partial n} = 0$	$\frac{\partial \omega}{\partial n} = 0$	Calculated
Distant field	$\frac{\partial v}{\partial n} = 0$	Reference pressure	$\frac{\partial k}{\partial n} = 0$	$\frac{\partial \omega}{\partial n} = 0$	Calculated
Blades	No-slip, MRF	$\frac{\partial p}{\partial n} = 0$	Wall function	Wall function	Wall function
Rim	No-slip, MRF	$\frac{\partial p}{\partial n} = 0$	Wall function	Wall function	Wall function
Hub	No-slip, MRF	$\frac{\partial p}{\partial n} = 0$	Wall function	Wall function	Wall function
Duct (rotating)	No-slip, counter-MRF	$\frac{\partial p}{\partial n} = 0$	Wall function	Wall function	Wall function
Duct (non-rotating)	No-slip, fixed	$\frac{\partial p}{\partial n} = 0$	Wall function	Wall function	Wall function

The grids of the computational domains are generated by the trimmed cell mesher in star ccm+. Obviously, the complete flow details need to be captured by encrypting the areas with a complex flow, including the RDT surface, wake field, leading edges and trailing edges. As for the grids near the wall, the prism layer mesher is selected for the full yplus wall treatment, which requires that yplus should be less than 5 or in the range of 30 to 300. Figure 4 shows the grids of the yoz cross-section and refined area.

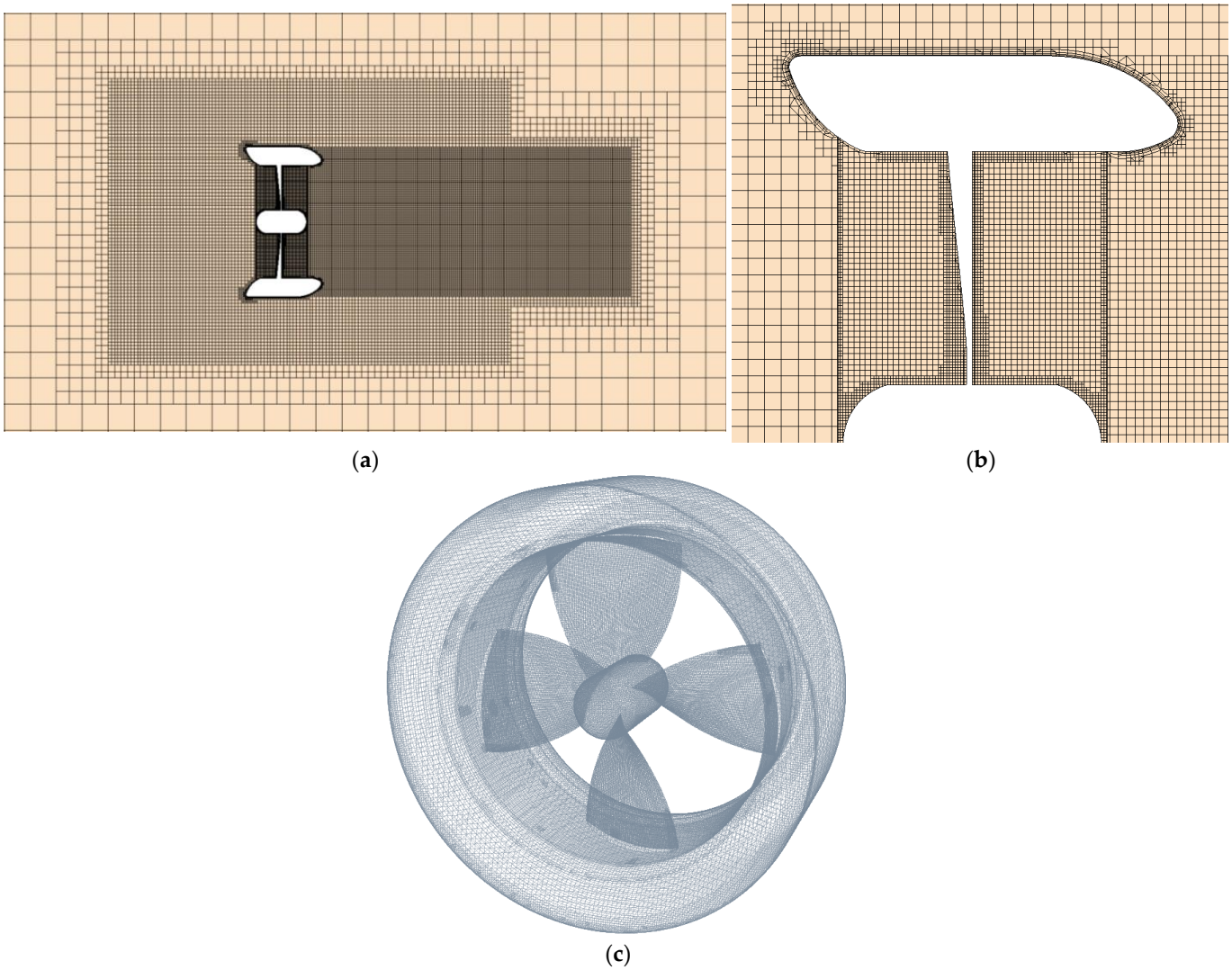

(**a**) (**b**)

(**c**)

Figure 4. Grid division of computing domains: (**a**) yoz cross section of static domain; (**b**) yoz cross section of rotating domain; (**c**) RDT surface.

Considering that the number of grids has a great impact on the calculation accuracy and efficiency, the six groups of grids shown in Table 3 are arranged for the sensitivity analysis based on the method proposed by Eça and Hoekstra at $J = 0.5$ [22,23]. This method takes the solution not within the so-called "asymmetric range" as the standard, which requires refining the grid beyond the allowable range in practical applications [18].

Table 3. Grid sensitivity analysis.

Configuration	Grids Count	KT_{Total}	ΔKT_{Total}	$10\ KQ_{Total}$	$10\ KQ_{Total}$
1-Very fine	14.03 million	0.3617	0	0.6241	0
2-Fine	6.42 million	0.36169	0.00%	0.62402	−0.01%
3-Medium	4.27 million	0.36152	−0.05%	0.6227	−0.22%
4-Reference	3.48 million	0.36181	0.03%	0.6253	0.19%
5-Coarse	1.53 million	0.35674	−1.37%	0.61314	−1.76%
6-Very coarse	0.86 million	0.34835	−3.69%	0.60053	−3.78%

The difference between the results of the different grid configurations and the asymptotic solution is within 4%, which shows that the RDT calculation results are considered reproducible. Secondly, the thrust difference and torque difference between the reference grid and the finest grid are 0.03% and 0.19%, respectively, which is sufficient for the subsequent optimization design. Therefore, this configuration will be selected in the study.

2.2.3. Verification of Calculation Method

Since the structure and hydrodynamic performance of the RDT are similar to those of the duct propeller, and the performance test of the duct propeller is relatively convenient and mature, the numerical calculation method will be verified by taking NO.19A + a Ka4-70 duct propeller as an example. The parameters of the duct propeller blades are shown in Table 4.

Table 4. Parameters of the duct propeller.

Diameter (m)	Number of Blades	Hub Ratio	Pitch Ratio	Disk Ratio	Rake Angle	Blade Profile
0.2	4	0.167	1.2	0.7	0°	NACA66

The hydrodynamic performance of the thruster can be defined in a dimensionless form as follows:

$$J = \frac{V_A}{nD},\ K_T = \frac{T}{\rho n^2 D^4},\ K_Q = \frac{Q}{\rho n^2 D^5},\ \eta = \frac{K_T}{Q_K} \times \frac{J}{2\pi} \tag{3}$$

where K_T is the thrust coefficient of the thruster, T is the thrust of the thruster, K_Q is the torque coefficient of the thruster, Q is the torque of the thruster, J is the advance coefficient, η is the efficiency of the thruster, V_A is the flow velocity, and n is the rotation speed of the blade.

As shown in Table 5 and Figure 5, the simulation values of the thrust coefficient, torque coefficient and open water efficiency are close to the test values, and their maximum errors are all less than 3%. This error is within the acceptable range, which indicates that the numerical calculation method adopted has high accuracy and can be used in the subsequent simulation.

Table 5. Comparison between the simulation and test of the duct propeller [24].

J	$K_{T\text{-sim}}$	$K_{T\text{-test}}$	$10\ K_{Q\text{-sim}}$	$10\ K_{Q\text{-test}}$	η_{sim}	η_{test}
0.2	0.5697	0.5632	0.65970	0.6531	0.2749	0.2745
0.3	0.5143	0.5044	0.63900	0.6341	0.3843	0.3798
0.4	0.4466	0.4467	0.60871	0.6073	0.4671	0.4683
0.5	0.3815	0.3879	0.57182	0.572	0.5309	0.5397
0.6	0.3183	0.3255	0.52859	0.5276	0.5750	0.5891
0.7	0.2564	0.2572	0.47757	0.473	0.5981	0.6058
0.8	0.1842	0.1807	0.41156	0.4071	0.5699	0.5652

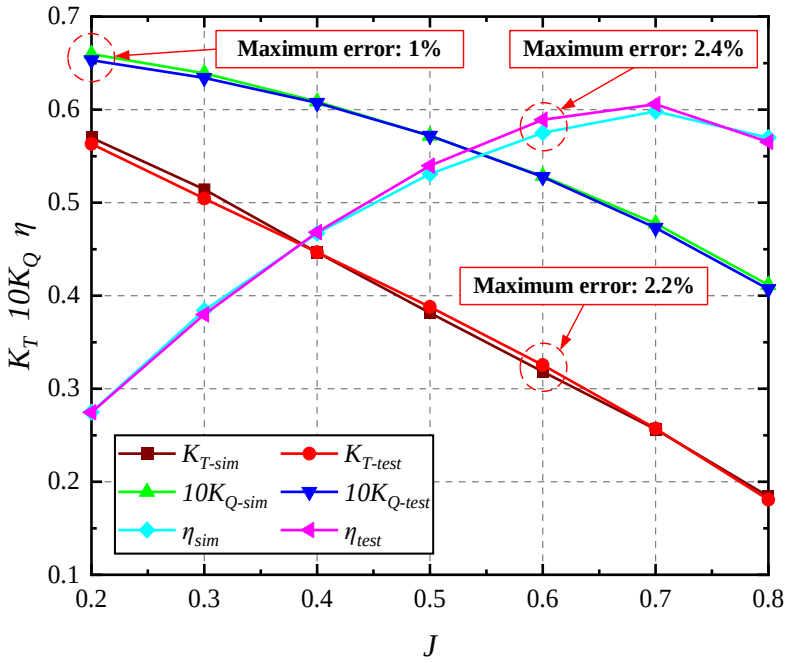

Figure 5. Comparison of the simulation and test results of the duct propeller.

2.3. Optimization Strategy

The aim of the response surface method is to fit the functional relationship between the target variables and the design variables by solving the multivariate high-order regression equation based on a series of sample points obtained through the appropriate experimental design method [25]. In general, when the highest order of the equation is the second order, the fitting result can fulfill the accuracy requirements [26]. According to the Taylor expansion polynomial and the variables selected in this paper, the functional relationship can be expressed as:

$$\overline{y} = \beta_0 + \sum_{i=1}^{3} \beta_i x_i + \sum_{i=1}^{3} \sum_{j=1}^{3} \beta_{ij} x_i x_j \tag{4}$$

where $\overline{y}$ is the fitting value of the target variable; x_i is the ith design variable; and β_0, β_i and β_{ij} are the regression coefficients.

In order to evaluate the accuracy of the fitting response surface, the determination coefficient R^2, the adjustment determination coefficient R^2_{ad}, the mean square σ_{RMSE} and the coefficient variability CV are selected to judge the prediction ability of the response surface model [27]. The expression of the evaluation index is as follows:

$$R^2 = 1 - \frac{\sum_{i=1}^{n_s} (y_i - \overline{y_i})^2}{\sum_{i=1}^{n_s} {y_i}^2 - \sum_{i=1}^{n_s} \overline{y_i}^2 / n_s} \tag{5}$$

$$R^2_{ad} = \frac{\left[\sum_{i=1}^{n_s} (y_i - \overline{y_i})^2\right] / (n_s - n_t - 1)}{\left(\sum_{i=1}^{n_s} {y_i}^2 - \sum_{i=1}^{n_s} \overline{y_i}^2 / n_s\right) / (n_s - 1)} \tag{6}$$

$$\sigma_{RMSE} = \sqrt{\frac{\sum_{i=1}^{n_s} (y_i - \overline{y_i})^2}{n_s}} \tag{7}$$

$$CV = \frac{\sigma_{RMSE}}{\sum_{i=1}^{n_s} y_i / n_s} \tag{8}$$

where $\overline{y}_i$ is the fitting value of the target point, y_i is the observation value of the target point, n_s is the number of sample points, n_t is the number of terms contained in the function polynomial, R^2 represents the correlation between the observed value and the fitted value of the target variable, R^2_{ad} represents the degree to which the response surface model explains the relationship between the target variable and the design variables, σ_{RMSE} represents the accuracy of the response surface model and CV represents the reproducibility of the response surface model.

The optimization of the RDT open water efficiency is taken as an example, and the procedure of the RSM is shown in Figure 6.

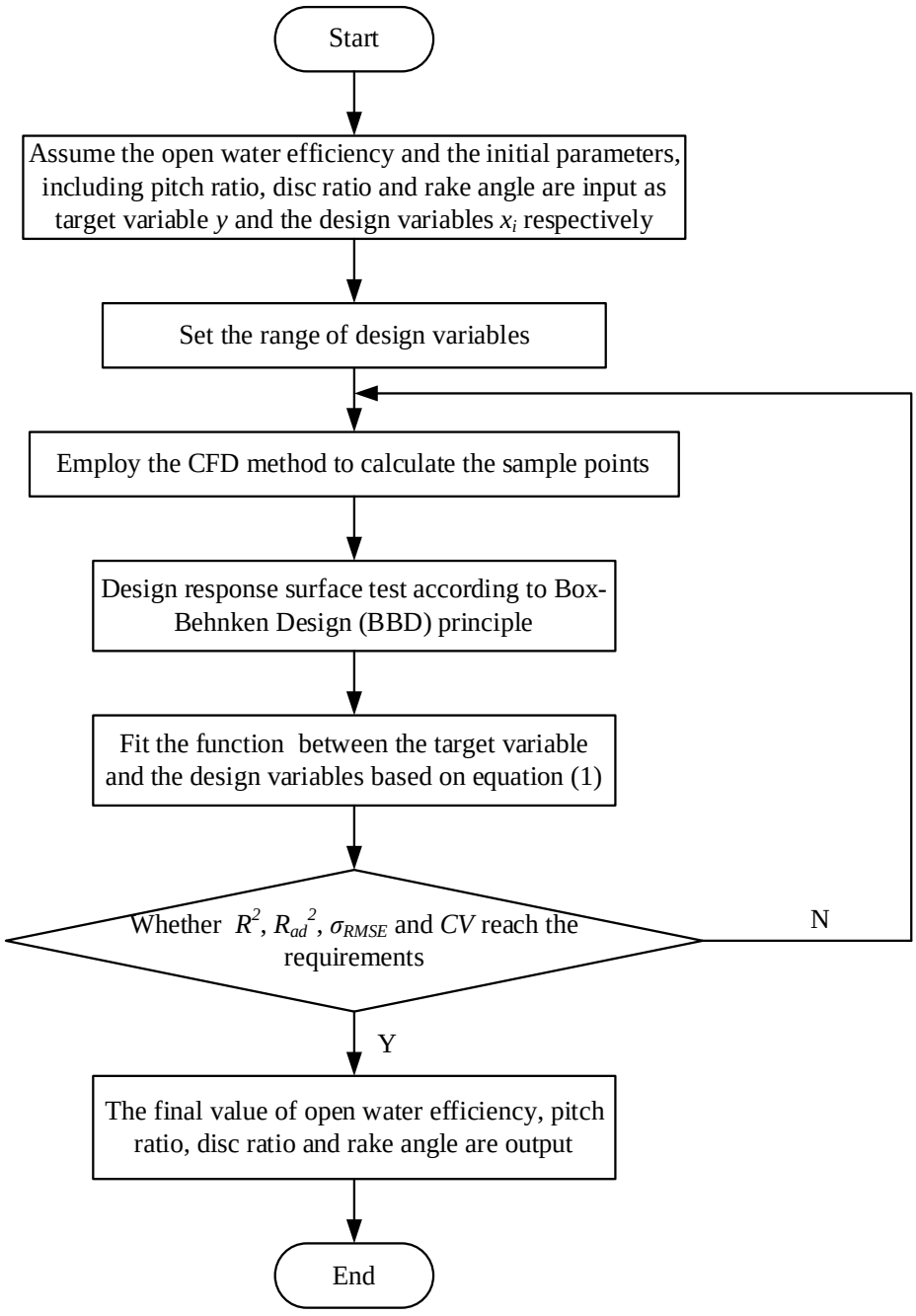

Figure 6. RSM procedure.

3. Optimization Parameters and Experimental Design

3.1. Parameters Selection

The pitch ratio is the ratio of the surface pitch P to the diameter D of the blade, which determines the spatial distribution and load distribution of the blade profile. According to the traditional propeller circulation theory, the closer the position of the maximum radial distribution of the blade load to the blade tip under the influence of the pitch ratio, the higher the blade efficiency, but the cavitation performance of the blade tip will be worse [28]. As for the disk ratio and rake angle, the disk ratio A_e/A_o is the ratio of the sum of the areas included in the blade extension profile to the propeller disk area, while the rake angle θ is the angle between the blade reference line and the vertical line of the axis. The disk surface ratio affects the efficiency and cavitation of the propeller by changing the blade thickness, chord and other structural parameters. The rake angle is designed to increase the distance between the blade and the stern to reduce the interference of the hull wake on the performance of the blade. However, the rake angle beyond the constraint range will increase the bending stress of the blade tip at the rim, thus reducing the blade strength. Therefore, these three parameters will be used as design variables to accomplish the collaborative optimization of open water efficiency. The geometric representation of different design variables is shown in Figure 7.

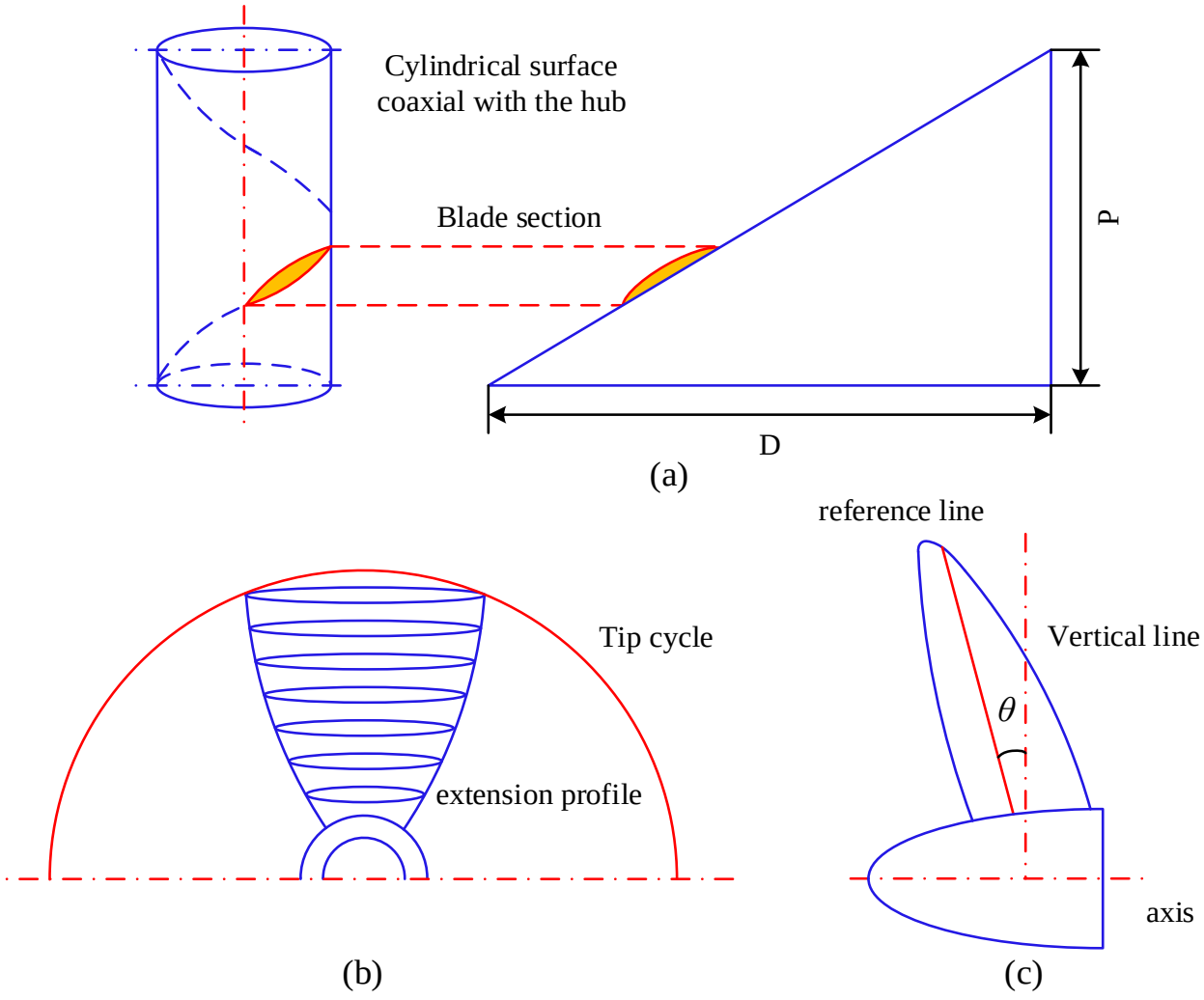

Figure 7. Geometric representation of the optimization parameters: (**a**) pitch ratio, (**b**) disk ratio and (**c**) rake angle.

3.2. Box–Behnken Experimental Design

The Box–Behnken design (BBD) is an experimental design type belonging to the RSM second-order model, which has better flexibility toward a small number of discontinuous variables compared with the central composite design. Moreover, depending on the specific working range of the structural parameters required by the RDT performance, this design type can fit the response surface without including high-level sample points composed of the upper and lower limits of various variables. The factor levels based on the BBD principle are shown in Table 6.

Table 6. Factors and levels affecting the open water efficiency.

Factor Name	Level		
	−1	**0**	**1**
Pitch ratio	1.0	1.2	1.4
Disk ratio	0.65	0.75	0.85
Rake angle/(°)	0	5	10

Within the above given parameter range, some RDT simulation data are supplemented to enrich the experimental data. The ultimate experimental data are fifteen groups, including two validation experiments, which can be carried out by setting the number of grids. The experimental scheme is shown in Table 7.

Table 7. Experimental scheme.

Case	X_1 Pitch Ratio	X_2 Disk Ratio	X_3 Rake Angle	Y Open Water Efficiency
1	1.0	0.65	5	40.98
2	1.4	0.65	5	51.77
3	1.0	0.85	5	38.49
4	1.4	0.85	5	49.75
5	1.0	0.75	0	41.05
6	1.4	0.75	0	52.48
7	1.0	0.75	10	39.9
8	1.4	0.75	10	50.88
9	1.2	0.65	0	48.32
10	1.2	0.85	0	47.85
11	1.2	0.65	10	46.91
12	1.2	0.85	10	46.62
13	1.2	0.75	5	47.41
14	1.2	0.75	5	46.87
15	1.2	0.75	5	47.23

4. Results and Discussion

4.1. Optimization Results

Through the regression fitting analysis of the experimental data in the table, the multivariate quadratic regression equation between the open water efficiency (Y) and the pitch ratio (X_1), the disk surface ratio (X_2) and the vertical inclination angle (X_3) can be obtained as follows:

$$\begin{gathered} Y = +47.17 + 5.5575X_1 - 0.65875X_2 - 0.67375X_3 + 0.1175X_1X_2 \\ -0.1125X_1X_3 + 0.045X_2X_3 - 1.635X_1^2 - 0.2875X_2^2 + 0.5425X_3^2 \end{gathered} \quad (9)$$

Table 8 presents the analysis of variance of the fitted response surface model according to the experimental data, in which the significance of the model and model terms is judged by the p-value or Prob > F-value related to the variance σ_{RMSE}. The p-value of the model is less than 0.0001, implying the regression model is significant. Values of "Prob > F" less than

0.05 indicate the model terms are significant. In this case, X_1, X_2, X_3 and ${X_1}^2$ are significant model terms. Comparing the significance (*p*-value) of each parameter, it can be seen that the influence of each structural parameter on the open water efficiency is in descending order of pitch ratio > rake angle > disk ratio. The "Lack-of-Fit F-value" of 7.83 implies the lack of fit is not significant relative to the pure error. There is a 11.54% chance that a "Lack-of-Fit F-value" this large could occur due to interference, which indicates that the model is reasonable.

Table 8. Variance analysis of the open water efficiency.

Source	Sum of Square	Degrees of Freedom	Mean Squared Error	F-Value	*p*-Value Prob > F
Model	266.00	9	29.56	76.70	<0.0001
X_1	247.09	1	247.09	641.21	<0.0001
X_2	3.47	1	3.47	9.01	0.0300
X_3	3.63	1	3.63	9.42	0.0278
X_1X_2	0.055	1	0.055	0.14	0.7206
X_1X_3	0.051	1	0.051	0.13	0.7318
X_2X_3	0.0081	1	0.0081	0.021	0.8904
${X_1}^2$	9.87	1	9.87	25.61	0.0039
${X_2}^2$	0.31	1	0.31	0.79	0.4143
${X_3}^2$	1.09	1	1.09	2.82	0.1539
residual	1.93	5	0.39		
lack of fit	1.78	3	0.59	7.83	0.1154
error	0.15	2	0.076		
sum	267.92	14			

In addition to the above significance test, the accuracy, reproducibility and anti-interference of the model should also be evaluated by the corresponding indicators. The correlation coefficient R^2 of the regression model is 99.28, indicating that the observed value of the target variable is strongly correlated with the fitted value. The prediction determination coefficient ${R^2}_{pred}$ = 89.27%, the adjustment determination coefficient ${R^2}_{adj}$ = 97.99% and the difference between the two indexes is less than 0.2, indicating that 97.99% of the change in the response value (open water efficiency) comes from the pitch ratio, disk surface ratio and rake angle. The coefficient of variation (CV) is 1.34% < 10%, indicating that the model has high repeatability and small variation. "Adeq precision" is 26.65 > 4, which indicates that the model has strong anti-interference and can be used to navigate the design space.

The response surface diagram and contour diagram of the design variables when they interact in pairs drawn according to Formula (9) are shown in Figure 8. It should be noted that, from the purple area to the red area, the minimum value of the efficiency gradually increases to the maximum value. Additionally, the influence of the interaction between different design parameters on the open water efficiency is embodied by the inclination of the three-dimensional map. If the inclination is greater, the influence will be more significant.

It can be seen that the combination of pitch ratio and disc ratio, as well as the combination of pitch ratio and rake angle, has a significant impact on the open water efficiency, while the combination of disc ratio and rake angle has little impact. The open water efficiency can be improved by increasing the pitch ratio and properly reducing the disc ratio and the rake angle, and the optimal value of efficiency is about 52%. In the circumstances, the pitch ratio is about 1.4, the disc ratio is between 0.62 and 0.72 and the rake angle is within the range of 0 to 2°. By searching the optimal value of the fitting function, the final optimization variables are obtained as follows: the pitch ratio is 1.4, the disc ratio is 0.651, the rake angle is 0° and the open water efficiency can reach 52.72%.

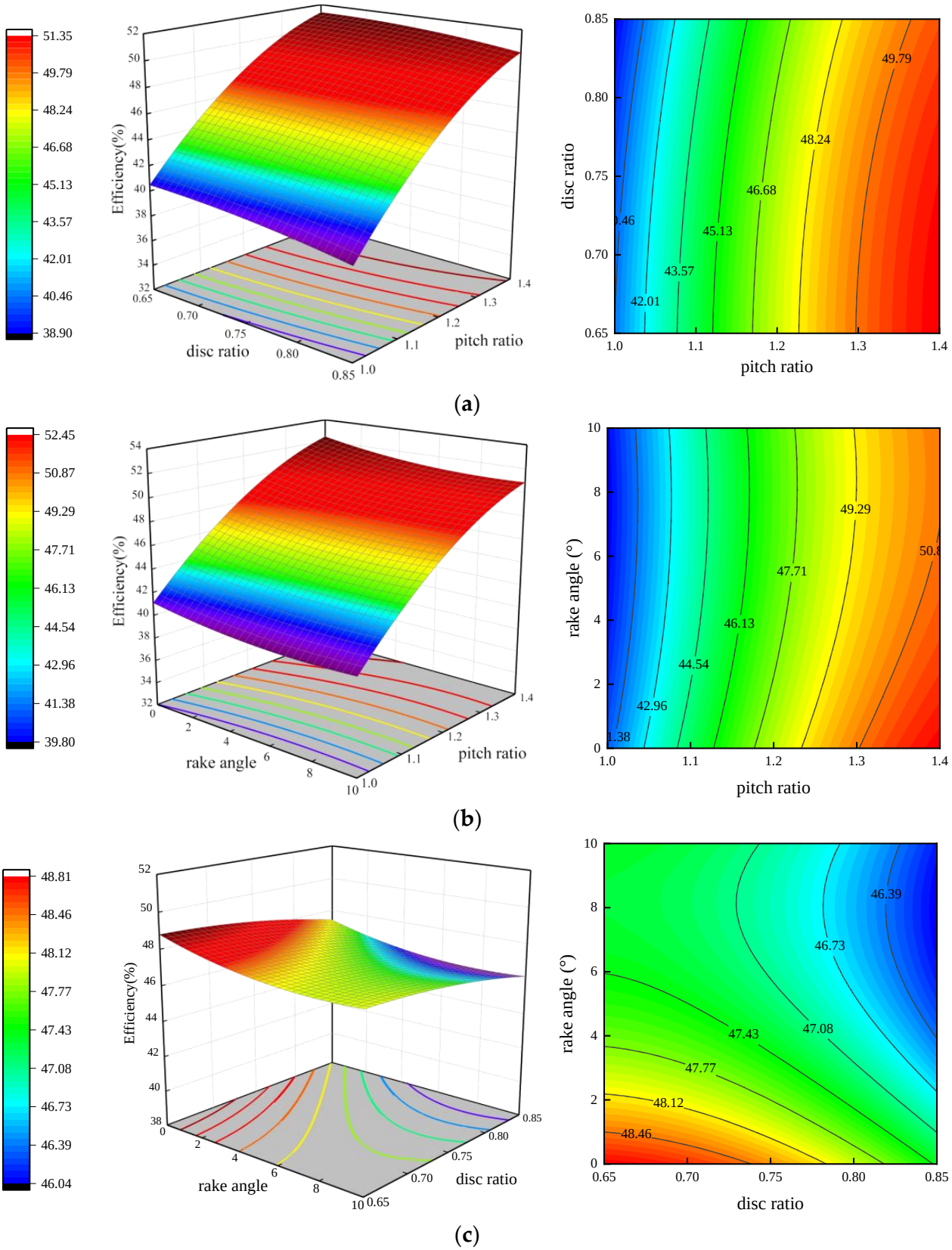

Figure 8. Interactions between different design variables. (**a**) Interactions between pitch ratio and disk surface ratio. (**b**) Interactions between pitch ratio and rake angle. (**c**) Interactions between disc ratio and rake angle.

4.2. Simulation Verification and Performance Comparison

To verify the response surface method, the optimization results will be compared with those calculated through the simulation. According to the optimal parameters recommended by the response surface optimization method, the model of a 1.4 pitch ratio, 0.651 disk surface ratio and 0° rake angle is shown in Figure 9.

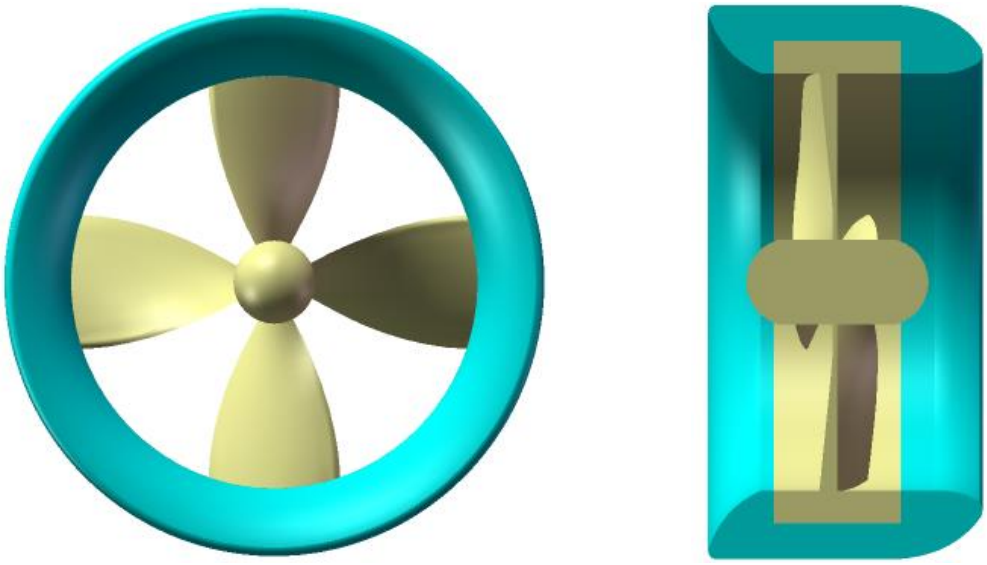

Figure 9. Optimized RDT model.

Table 9 shows the comparison of the simulation results between the prototype RDT and optimized RDT. The maximum efficiency of the optimized RDT is 52.53% at about J = 0.7. The error between the highest efficiency predicted by the response surface and the simulation result is 0.19%, which indicates that the analysis results are quite consistent with the simulation values, and the equation fitted by RSM can accurately reflect the influence of multi-parameter synergy on the open water efficiency of RDT. Compared with the prototype RDT, the maximum open water efficiency is effectively improved by 13.8%. Considering that the efficiency of the RDT mainly depends on the thrust and torque generated by the pressure difference between the suction surface and the pressure surface of the blades, the pressure distribution of the prototype RDT and the optimized RDT shown in Figure 10 will be adopted to further discuss the reasons for the efficiency improvement.

Table 9. Comparison of the simulation results between the prototype RDT and optimized RDT.

J	V_A (m/s)	Prototype RDT			Optimized RDT		
		$K_{T\text{-pro}}$	10 $K_{Q\text{-pro}}$	η_{pro}	$K_{T\text{-opt}}$	10 $K_{Q\text{-opt}}$	η_{opt}
0.4	1.5253	0.4797	0.8353	0.3656	0.6151	0.9590	0.4083
0.5	1.9067	0.4255	0.8104	0.4178	0.5454	0.9362	0.4636
0.6	2.288	0.3649	0.7772	0.4484	0.4768	0.9068	0.5021
0.7	2.670	0.3043	0.7346	0.4615	0.4075	0.8692	0.5253
0.8	3.051	0.2393	0.6802	0.4479	0.3341	0.8209	0.5183
0.9	3.432	0.1643	0.6124	0.3843	0.2553	0.7611	0.4805
1.0	3.813	0.0943	0.5378	0.2791	0.1704	0.6890	0.3936

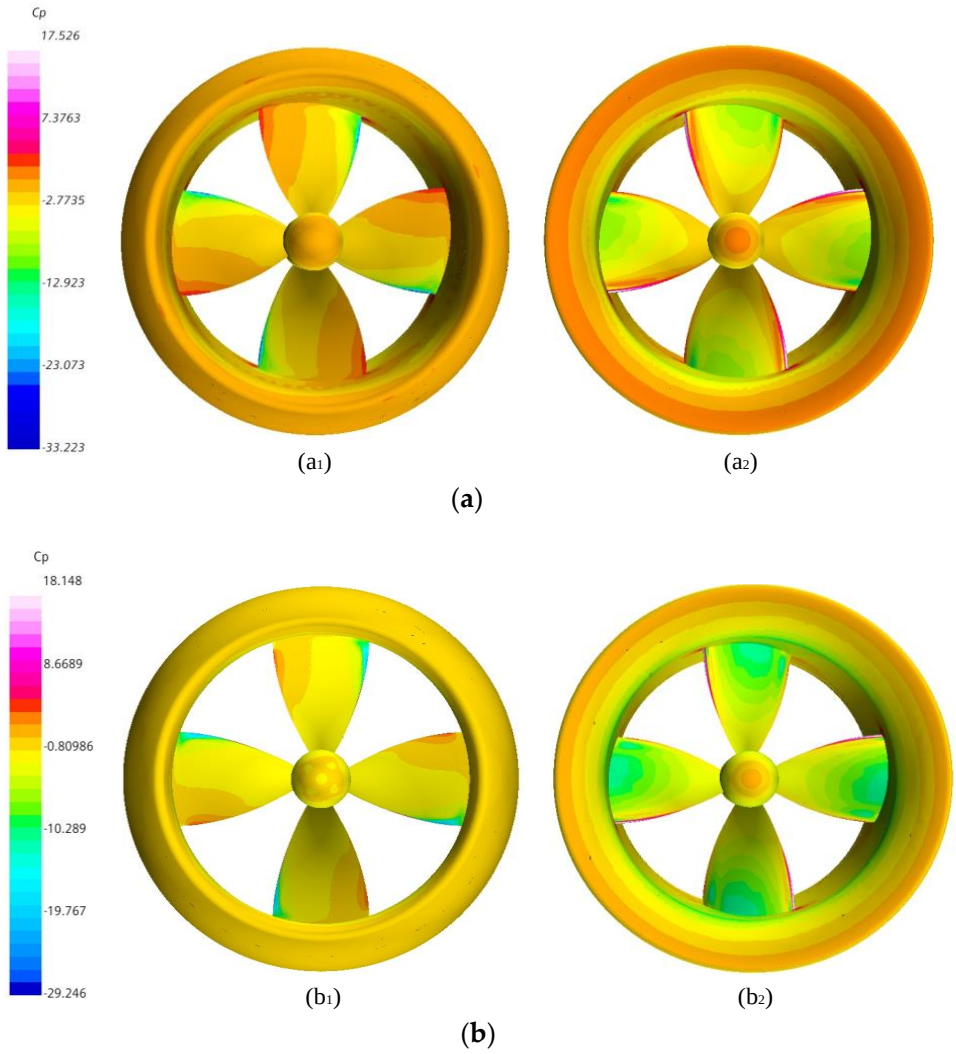

Figure 10. Pressure distribution of the RDT. (**a**) Prototype RDT. (**b**) Optimized RDT.

As shown in Figure 10, the pressure coefficient C_p is used to describe the hydrodynamic load distribution on the RDT surface, which can be defined as:

$$C_p = \frac{P - P_\infty}{\frac{1}{2}\rho {V_A}^2} \tag{10}$$

where P is the local pressure, and P_∞ is the free stream pressure.

It can be observed that the pressure distribution on the suction side of the optimized RDT is more significantly improved than that on the pressure side, which is a crucial factor for improving the efficiency. In addition, the pressure coefficient on the pressure side of the two RDTs increases in sequence from the leading edge to the trailing edge, while the pressure coefficient on the suction side decreases first and then increases in this direction. As a result, there is a negative pressure area near the leading edge on the pressure side and a positive pressure area near the leading edge and the trailing edge on the suction side. Although the thrust loss has been effectively reduced through optimization, the reverse pressure zone is still obvious, which indicates that the efficiency of the optimized RDT can be further improved.

To gain insight into the pressure distribution on the blade surface, the pressure coefficients of different radius profiles are shown in Figure 11. As can be seen, the pressure distribution curves of the suction surface and pressure surface intersect from 0.3 R to 0.9 R. Obviously, the effective thrust is generated by the pressure difference between the

two curves on the left side of the intersection, but the adverse thrust is also caused by the pressure difference of the right curves. It is observed that the thrust loss gradually increased from blade root to blade tip, especially after 0.5 R. Therefore, the thrust can be raised by optimizing the blade profile after 0.5 R.

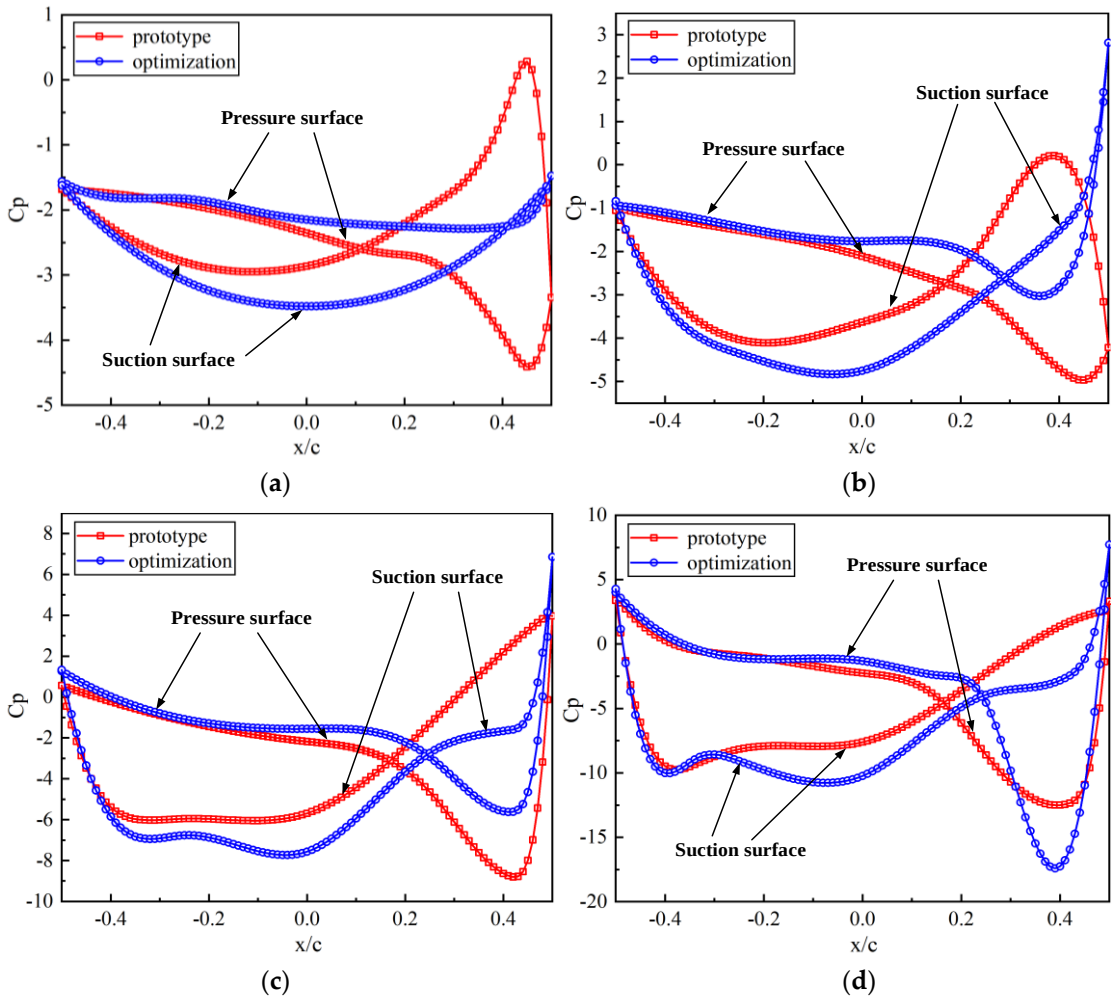

Figure 11. Pressure coefficient at different sections (J = 0.7): (**a**) 0.3 R, (**b**) 0.5 R, (**c**) 0.7 R and (**d**) 0.9 R.

Since the performance of the RDT is directly related to the characteristics of the flow field, the nondimensional axial velocity distribution in different planes shown in Figure 12 is used to depict the changes of the flow field structure, including the plane at z/R = ±0.2 before and after the propeller disk and the yoz plane. From Figure 12a_2,a_3,b_2,b_3, it can be observed that the pressure-driven flow in the axial direction develops a significant velocity gradient along the radial direction, whether upstream or downstream of the blades. However, the optimized RDT has a smaller velocity gradient and wake velocity compared with the prototype RDT, which indicates that the flow field in the rotating region becomes more uniform, and less energy is lost in the wake with the improvement of the performance. In addition, there is an obvious velocity difference around the wake of the nozzle and the hub, where flow separation occurs under the action of shear stress. To better illustrate this phenomenon in the wake field, the iso-surface with a Q-factor equal to 600 s^{-2} is shown in Figure 13. It should be pointed out here that, since the velocity field and vorticity are in good consistency in the steady calculations, the flow separation phenomenon can be clarified by the Q-factor in the wake. However, this approach is not applicable to unsteady simulations [29].

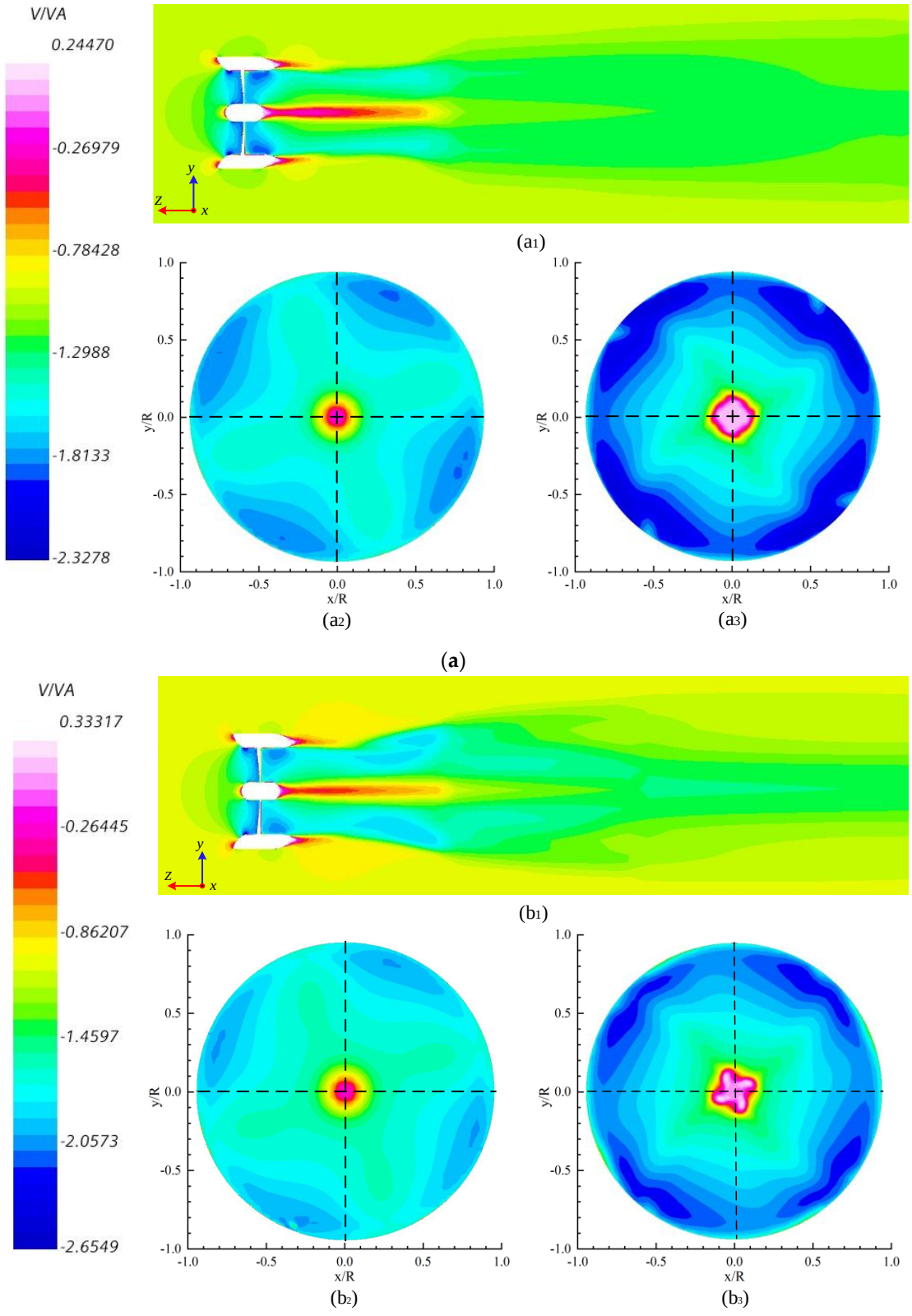

Figure 12. Nondimensional axial velocity distribution of the RDT flow field. (**a**) Prototype RDT. (**b**) Optimized RDT.

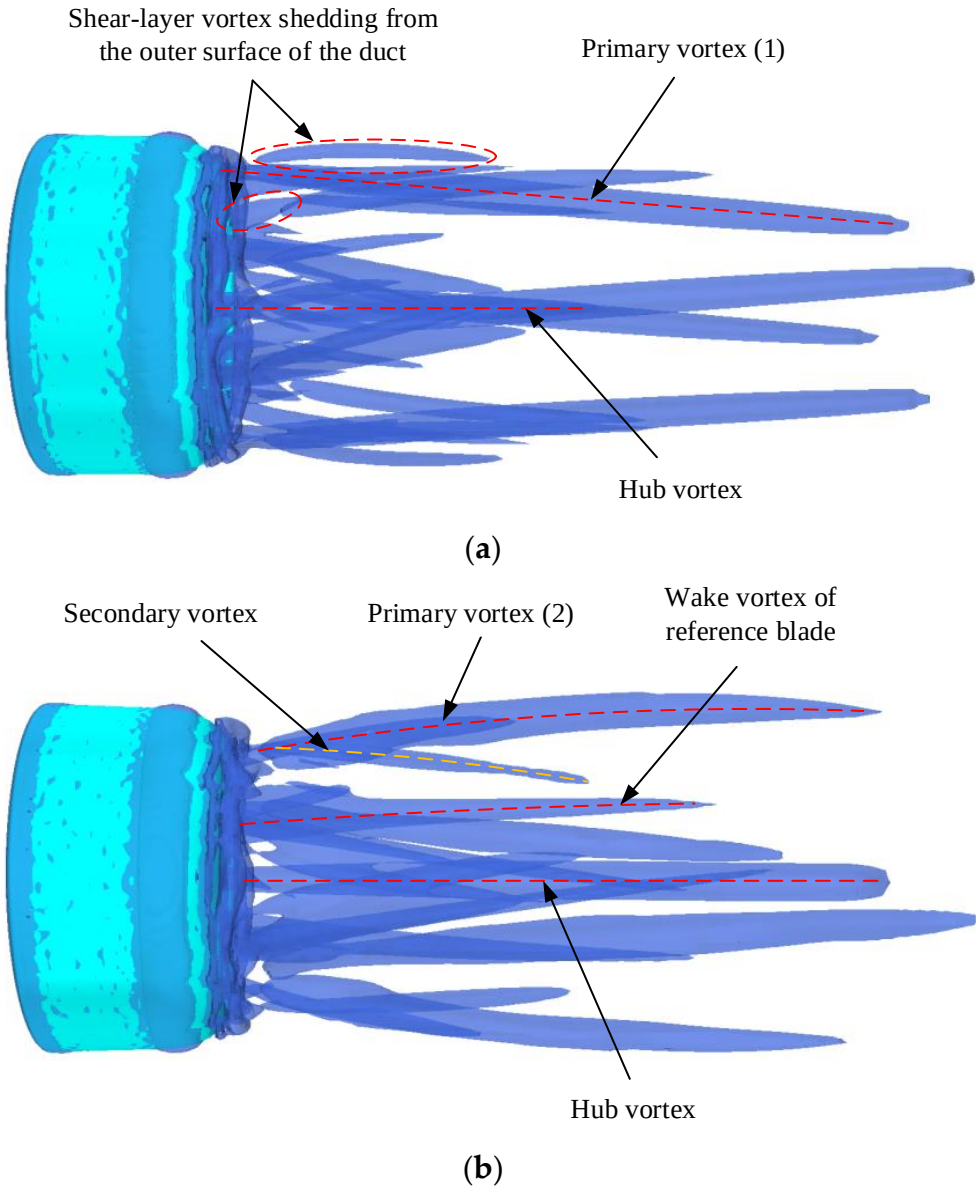

Figure 13. Vortical structures of the RDT wake. (**a**) Prototype RDT. (**b**) Optimized RDT.

Due to the interaction between the decelerating flow from the duct boundary layer and the wake from the blades, some obvious vortices are generated at the trailing edge of the duct, which are defined as the primary vortex (1) and primary vortex (2) in Figure 13a,b. Obviously, the primary vortex (2) has a higher strength, and a secondary vortex is derived, which is consistent with the stronger flow separation around the wake of the duct nozzle shown in Figure 12b$_1$. Moreover, the shear layer vortex can hardly be observed in the optimized RDT, while the wake vortex of the blade is more obvious than that of the prototype RDT. This is because the improvement of the efficiency enhances the energy of the wake vortex, making its dissipation process longer. Nevertheless, there is still a strong separation vortex at the nozzle of the optimized RDT; thus, the structure can be optimized to improve the distribution and strength of the wake field.

5. Conclusions

In this paper, a multi-parameter collaborative optimization framework is proposed to improve the efficiency of RDT. The main conclusions are as follows:

(1) The p-value of the model is less than 0.0001, and the Lack-of-Fit F-value, correlation coefficient R^2, prediction determination coefficient R^2_{pred}, adjustment determination coefficient R^2_{adj}, coefficient of variation CV and Adeq precision are 7.83, 99.28, 89.27%, 97.99%, 1.34% and 26.65, respectively, indicating that the established model has high precision, good reproducibility and strong anti-interference ability.
(2) The influence of the pitch ratio, rake angle and disk ratio on the open water efficiency decreases in sequence. The pitch ratio has a significant effect on the open water efficiency, while the rake angle and disk ratio have little effect.
(3) Compared with the prototype RDT, the maximum efficiency of the optimized RDT is increased by 13.8%. Additionally, the surface pressure distribution and flow field characteristics are significantly modified, but the efficiency can be further improved by optimizing the local structure.

Author Contributions: Conceptualization, Y.N. and W.O.; methodology, Y.N. and W.O.; software, Y.N.; validation, Y.N., W.O. and Z.Z.; formal analysis, Z.Z.; investigation, G.L.; resources, G.L.; data curation, Y.N.; writing—original draft preparation, Y.N.; writing—review and editing, W.O. and Z.Z.; visualization, R.Z.; supervision, W.O.; project administration, W.O.; funding acquisition, W.O. All authors have read and agreed to the published version of the manuscript.

Funding: This project was financially supported by National Key Research and Development Project of China (No. 2018YFE0197600 and No. 2022YFB4300800) and the European Union's Horizon 2020 Research and Innovation Programme RISE under grant agreement No. 823759, REMESH. This research received no external funding.

Data Availability Statement: Not applicable.

Conflicts of Interest: The authors declare no conflict of interest.

References

1. Nguyen, H.P.; Hoang, A.T.; Nizetic, S.; Nguyen, X.P.; Le, A.T.; Luong, C.N.; Chu, V.D.; Pham, V.V. The electric propulsion system as a green solution for management strategy of CO2 emission in ocean shipping: A comprehensive review. *Int. Trans. Electr. Energy Syst.* **2021**, *31*, e12580. [CrossRef]
2. Hansen, J.F.; Wendt, F. History and state of the art in commercial electric ship propulsion, integrated power systems, and future trends. *Proc. IEEE* **2015**, *103*, 2229–2242. [CrossRef]
3. Yan, X.; Liang, X.; Ouyang, W.; Liu, Z.; Liu, B.; Lan, J. A review of progress and applications of ship shaft-less rim-driven thrusters. *Ocean Eng.* **2017**, *144*, 142–156. [CrossRef]
4. Liang, X.; Yan, X.; Ouyang, W.; Liu, Z. Experimental research on tribological and vibration performance of water-lubricated hydrodynamic thrust bearings used in marine shaft-less rim driven thrusters. *Wear* **2019**, *426*, 778–791. [CrossRef]
5. Zhu, Z.; Liu, H. The external characteristics and inner flow research of rim-driven thruster. *Adv. Mech. Eng.* **2022**, *14*, 16878132221081608. [CrossRef]
6. Freeman, M.D.; Marshall, M.A. An analytical investigation into the design of a shaftless thruster using finite element and computational fluid dynamics approaches. *J. Ocean. Technol.* **2011**, *6*, 55–68.
7. Chen, Y.; Wang, L.; Hua, H.X. Longitudinal vibration and unsteady thrust transmission of the rim driven thruster induced by ingested turbulence. *Ocean Eng.* **2017**, *131*, 149–161. [CrossRef]
8. Jiang, H.; Ouyang, W.; Sheng, C.; Lan, J.; Bucknall, R. Numerical investigation on hydrodynamic performance of a novel shaftless rim-driven counter-rotating thruster considering gap fluid. *Appl. Ocean Res.* **2022**, *118*, 102967. [CrossRef]
9. Yang, J.; He, W.; Li, Z. On Scale Effect of Rim-Driven Thruster Based on RANS Method. In Proceedings of the 30th International Ocean and Polar Engineering Conference, Virtual, 11–16 October 2020; OnePetro: Richardson, TX, USA, 2020.
10. Kinnas, S.A.; Chang, S.H.; He, L.; Johannessen, J.T. Performance prediction of a cavitating RIM driven tunnel thruster. In Proceedings of the First International Symposium on Marine Propulsors, Trondheim, Norway, 22–24 June 2009.
11. Cai, B.; Tian, B.; Qiu, L.; Xu, Q.; Mao, X.; He, W.; Chai, W. Application of the body force method in the rim driven thruster. *Int. J. Nav. Archit. Ocean Eng.* **2022**, *14*, 100476. [CrossRef]
12. Hieke, M.; Sultani, H.; Witte, M.; von Estorff, O.; Wurm, F.H. A workflow for hydroacoustic source analyses based on a scale-resolving flow simulation of a hubless propeller. *Ocean Eng.* **2022**, *261*, 112131. [CrossRef]
13. Zhang, S.; Zhu, X.; Zhou, Z.L. Hydrodynamic performance analysis of hubless rim-driven propulsors. *Appl. Mech. Mater.* **2013**, *256*, 2565–2568. [CrossRef]
14. Xiancheng, S.; Guoping, Z.; Liwei, Y.; Zengwu, Z.; Guanzhi, T.; Jingguo, Y. Research on the influence of endwall on the hydrodynamic performance of shaftless rim-driven thruster. In Proceedings of the CSAA/IET International Conference on Aircraft Utility Systems (AUS 2020), Online, 18–21 September 2020; IET: London, UK, 2020; Volume 2020, pp. 1190–1195.

15. Cao, Q.M.; Hong, F.W.; Tang, D.H.; Hu, F.L.; Lu, L.Z. Prediction of loading distribution and hydrodynamic measurements for propeller blades in a rim driven thruster. *J. Hydrodyn.* **2012**, *24*, 50–57. [CrossRef]
16. Liu, B.; Vanierschot, M.; Buysschaert, F. Effects of transition turbulence modeling on the hydrodynamic performance prediction of a rim-driven thruster under different duct designs. *Ocean Eng.* **2022**, *256*, 111142. [CrossRef]
17. Cai, M.; Yang, C.; Wu, S.; Zhu, Y.; Xie, Y. Hydrodynamic analysis of a rim-driven thruster based on RANS method. In Proceedings of the OCEANS 2015-MTS/IEEE Washington Conference, Washington, DC, USA, 19–22 October 2015; IEEE: New York, NY, USA, 2015; pp. 1–5.
18. Gaggero, S. Numerical design of a RIM-driven thruster using a RANS-based optimization approach. *Appl. Ocean Res.* **2020**, *94*, 101941. [CrossRef]
19. Song, B.; Wang, Y.; Tian, W. Open water performance comparison between hub-type and hubless rim driven thrusters based on CFD method. *Ocean Eng.* **2015**, *103*, 55–63. [CrossRef]
20. CD-Adapco. User Guide STAR-CCM+ Version 9.0.2. 2014. Available online: https://vdocuments.mx/star-ccm-user-guide.html (accessed on 1 December 2022).
21. Menter, F.R. Two-equation eddy-viscosity turbulence models for engineering applications. *AIAA J.* **1994**, *32*, 1598–1605. [CrossRef]
22. Eça, L.; Hoekstra, M. Evaluation of numerical error estimation based on grid refinement studies with the method of the manufactured solutions. *Comput. Fluids* **2009**, *38*, 1580–1591. [CrossRef]
23. Eça, L.; Hoekstra, M. A procedure for the estimation of the numerical uncertainty of CFD calculations based on grid refinement studies. *J. Comput. Phys.* **2014**, *262*, 104–130. [CrossRef]
24. Zhao, Q. CFD Simulation of Performance for Duct Propeller and Ship Wake. Ph.D. Thesis, Wuhan University of Technology, Wuhan, China, 2011.
25. Chelladurai, S.J.S.; Murugan, K.; Ray, A.P.; Upadhyaya, M.; Narasimharaj, V.; Gnanasekaran, S. Optimization of process parameters using response surface methodology: A review. *Mater. Today: Proc.* **2021**, *37*, 1301–1304. [CrossRef]
26. Jones, D.R. A taxonomy of global optimization methods based on response surfaces. *J. Glob. Optim.* **2001**, *21*, 345–383. [CrossRef]
27. Myers, R.H.; Montgomery, D.C.; Anderson-Cook, C.M. *Response Surface Methodology: Process and Product Optimization Using Designed Experiments*; John Wiley & Sons: Hoboken, NJ, USA, 2016.
28. Zhenbang, S.; Yingzhong, L. *Ship Principle*, 1st ed.; Shanghai JiaoTong University Press: Shanghai, China, 2004; p. 1.
29. Li, D.; Zhang, N.; Jiang, J.; Gao, B.; Alubokin, A.A.; Zhou, W.; Shi, J. Numerical investigation on the unsteady vortical structure and pressure pulsations of a centrifugal pump with the vaned diffuser. *Int. J. Heat Fluid Flow* **2022**, *98*, 109050. [CrossRef]